Applied Physics A (2022) 128:142
https://doi.org/10.1007/s00339-022-05289-3

Applied Physics A
Materials Science & Processing

Optical and electrical properties of $Al_{1-x}In_xN$ films with a wide middle-composition range by RF sputtering

JianJin Chen[1] · DongLi Qi[1] · XueFei Li[2] · JianYu Song[1] · LongHai Shen[1]

Received: 13 October 2021 / Accepted: 12 January 2022 / Published online: 22 January 2022

Abstract

$Al_{1-x}In_xN$ films with a wide middle-composition range were deposited on Si/glass substrate by radio-frequency magnetron sputtering. The microstructures of as-grown $Al_{1-x}In_xN$ films were characterised by AFM, SEM, and EDS. The optical bandgap of $Al_{1-x}In_xN$ films can be tuned from 1.85 to 2.93 eV by decreasing the In content from 0.7 to 0.3, covering the whole visible region. Raman spectroscopy demonstrates A_1 and E_2 (high) phonon modes in the $Al_{1-x}In_xN$ films. The photoluminescence spectra of $Al_{1-x}In_xN$ films reveals the emission band originates from the band edge-related radiation. The optical bowing parameter of $Al_{1-x}In_xN$ films is confirmed to be 2.28 eV. The conductivity of the films increases with increasing In content. The I-V curves show the $Al_{1-x}In_xN$ films form quasi-Ohmic contact with W electrodes.

Keywords $Al_{1-x}In_xN$ films · Magnetron sputtering · Optical bandgap · I-V characteristics

1 Introduction

Group III-nitride alloy semiconductors have attracted considerable attention because of their huge economic benefits when used in applications such as light-emitting diodes (LED), laser diodes, photodetectors, high-power electronic devices, renewable hydrogen energy systems and surface acoustic wave (SAW) devices [1–6]. In particular, AlInN alloys possess the widest adjustable bandgap covering the spectrum from deep-ultraviolet to near-infrared wavelengths via changing the content ratio of Al/In [7]. Thanks to their extraordinarily tunable bandgap, AlInN films have shown potential application in multi-junction tandem solar cells, photoelectrochemical solar water splitting, deep-ultraviolet and visible polarised light emitters [8, 9]. Therefore, numerous strategies have been discovered to realise the growth of $Al_{1-x}In_xN$ films with tunable compositions, including metal–organic chemical vapour deposition (MOCVD) [10–13], radio-frequency metal–organic molecular beam epitaxy (RF-MOMBE) [14], and plasma-assisted dual source reactive evaporation [9, 15, 16]. However, among these techniques, the In content of $Al_{1-x}In_xN$ films can only be adjusted in a small range owing to the phase separation caused by the high growth temperature. As one of the low-temperature growth techniques, reactive magnetron sputtering is an effective method for the growth of single-phase $Al_{1-x}In_xN$ films with fully tunable composition ($0 < x < 1$) [17–23], which offers a platform for the study of the optical and electrical properties of $Al_{1-x}In_xN$ films with different compositions. At present, there are few reports on the investigation of PL mechanism by comparing the optical transmission and PL spectra of the $Al_{1-x}In_xN$ films with wide middle composition. Furthermore, previous studies revealed the curves of optical bandgap (E_g) dependence on In composition show different deviations from Vegard's law due to using different E_g values of InN and AlN [15, 22, 24]. The bandgap bowing parameter obtained using experimental E_g of $Al_{1-x}In_xN$ films with middle composition will be reasonable to determine the correlation of factual E_g with the In composition. The bowing parameter obtained in this study is less than the reported values, which reasonably predict the factual E_g of Al-rich and In-rich $Al_{1-x}In_xN$ films prepared by magnetron sputtering. Therefore, investigating and comparing the dependence of optical and electrical properties on In

✉ DongLi Qi
285385997@qq.com

✉ LongHai Shen
shenlonghai@163.com

[1] School of Science, Shenyang Ligong University, Shenyang 110159, China

[2] Key Laboratory of Functional Materials Physics and Chemistry of the Ministry of Education, Jilin Normal University, Changchun 136000, China

composition for $Al_{1-x}In_xN$ films is conducive to expansion of the requirement for variety among spectral-responsive optoelectronic devices.

Here, we study the microstructure, optical transmittance, photoluminescence (PL), and electrical properties of single-phase $Al_{1-x}In_xN$ films ($0.3 \le x \le 0.7$) deposited by radio-frequency magnetron sputtering (RF-MS). The dependent relations of microstructure, optical bandgap, and current–voltage (*I-V*) characteristics on the In content of $Al_{1-x}In_xN$ films are investigated. The optical bandgap can be tuned within the visible light range (1.85–2.93 eV) and the bowing parameters are estimated.

2 Experimental work

The $Al_{1-x}In_xN$ films were grown on single crystal Si (100) and glass substrates under the same deposition conditions by RF-MS. The Al target was partially covered by In blocks (99.999%; size ≤ 8 mm). The In content of $Al_{1-x}In_xN$ films was tuned by varying the number of In blocks. Before deposition, the Si and glass substrates were ultrasonically cleaned in alcohol, rinsed with de-ionised water, and then dried using argon gas. The substrates were etched using pure Ar (99.999%) plasma at a pressure of 30 Pa for 15 min under a substrate temperature of 350 ℃ to remove surface contaminants. The chamber was evacuated to a base pressure of less than 5×10^{-4} Pa. Before $Al_{1-x}In_xN$ film deposition, the target was pre-sputtered for 15 min to remove surface contaminants. The $Al_{1-x}In_xN$ films were then deposited on the substrates using an RF power of 300 W with a substrate temperature of 350 ℃ for 2 h. The sputtering pressure, Ar/N_2 flow ratio and target–substrate distance were 1 Pa, 54:36 sccm, and 70 mm, respectively.

The crystal structure and surface morphology of the samples were characterised by X-ray diffraction (XRD, Hitachi D/max2500PC) with Cu Kα radiation ($\lambda = 0.15418$ nm), scanning electron microscopy (SEM, MAIA3 TESCAN), and atomic force microscopy (AFM, Dimension Icon, Bruker), respectively. Energy-dispersive X-ray spectroscopy (EDS) equipment attached to the SEM was used to measure the elemental compositions of the samples. The optical transmittance of the films prepared on the glass substrate was measured by an UV–Vis-NIR spectrometer (Lambda 950, PerkinElmer). The optical properties of the as-prepared $Al_{1-x}In_xN$ films were performed by the Renishaw Raman spectroscopy at room temperature with an Ar^+ ion laser at 514.5 nm as the excitation source. The photoluminescence (PL) was acquired using Renishaw inVia™ spectroscopy with a 325-nm laser at room temperature. The carrier concentration of prepared $Al_{1-x}In_xN$ films was obtained by ECOPIA Hall Effect Measurement System (HMS-500). The electrical properties of the films grown on the glass substrate were measured by probe station equipped with a Semiconductor Characterisation System (Keithley 4200-SCS). The metal W needle was used as contact electrode.

3 Results and discussion

$Al_{1-x}In_xN$ films as study samples were obtained from our previous study involving the use of RF-MS [25]. The XRD patterns of as-grown $Al_{1-x}In_xN$ films showed that the In content x was tuned over a wide range of 0.3 to 0.7 (Figure S1, Supporting Information). The root-mean-squared (RMS) roughness of $Al_{1-x}In_xN$ films with different In contents was calculated through AFM Nanoscope software. The AFM images of $Al_{1-x}In_xN$ films on Si substrate are shown in Fig. 1a–e. The RMS surface roughness of $Al_{1-x}In_xN$ films is 2.53, 4.31, 4.54, 7.45, and 2.39 nm, corresponding to In content x of 0.3, 0.55, 0.59, 0.64, and 0.7, respectively. The $Al_{1-x}In_xN$ alloy films show relatively smooth surface morphologies with an average RMS roughness of 4.2 nm. The roughness increases with increasing In content ($x = 0.3 \sim 0.64$) and then significantly decreases at In content of $x = 0.7$. The low surface roughness 2.53 and 2.39 nm are obtained in Al-rich ($x = 0.3$) and In-rich ($x = 0.7$) $Al_{1-x}In_xN$ films, respectively. The $Al_{0.3}In_{0.7}$ N film exhibits the lowest surface roughness, owing to the higher mobility of In adatoms than Al adatoms. When the Al and In content have small differences in $Al_{1-x}In_xN$ films, the formation of big granular with distinct grain boundaries obviously results in the increase in the RMS roughness. This may be attributed to increased competition of Al and In adatoms, because neither adatom is dominant on the surface.

The distribution of element across the $Al_{1-x}In_xN$ films was analysed by EDS. Figure 2 illustrates the elemental mapping of surface SEM images for three typical $Al_{1-x}In_xN$ films with In contents of $x = 0.3$, 0.59, and 0.7, respectively. It can be observed that the distribution of Al, In, and N is relatively uniform for as-grown $Al_{1-x}In_xN$ films. The compositional homogenisation for the cross section of $Al_{1-x}In_xN$ films is further confirmed by line-scan EDS for two typical $Al_{1-x}In_xN$ films with In contents of $x = 0.55$ and 0.59, as shown in Fig. 3. The elements Al, In, and N are uniformly distributed along the cross-sectional direction of $Al_{1-x}In_xN$ films.

The optical bandgap energy (E_g) dependence on In content of $Al_{1-x}In_xN$ films was evaluated by analysing transmission spectra measurements. Figure 4a shows the transmission spectra of $Al_{1-x}In_xN$ films with different In contents. With the increase in In content, the absorption edge of the $Al_{1-x}In_xN$ films shifts towards a longer wavelength and the transmittance intensity of $Al_{1-x}In_xN$ films gradually decreases. The fact that the absorption edge of $Al_{1-x}In_xN$ films shifts towards a longer wavelength is attributed to the variation of the E_g, which will be further investigated later.

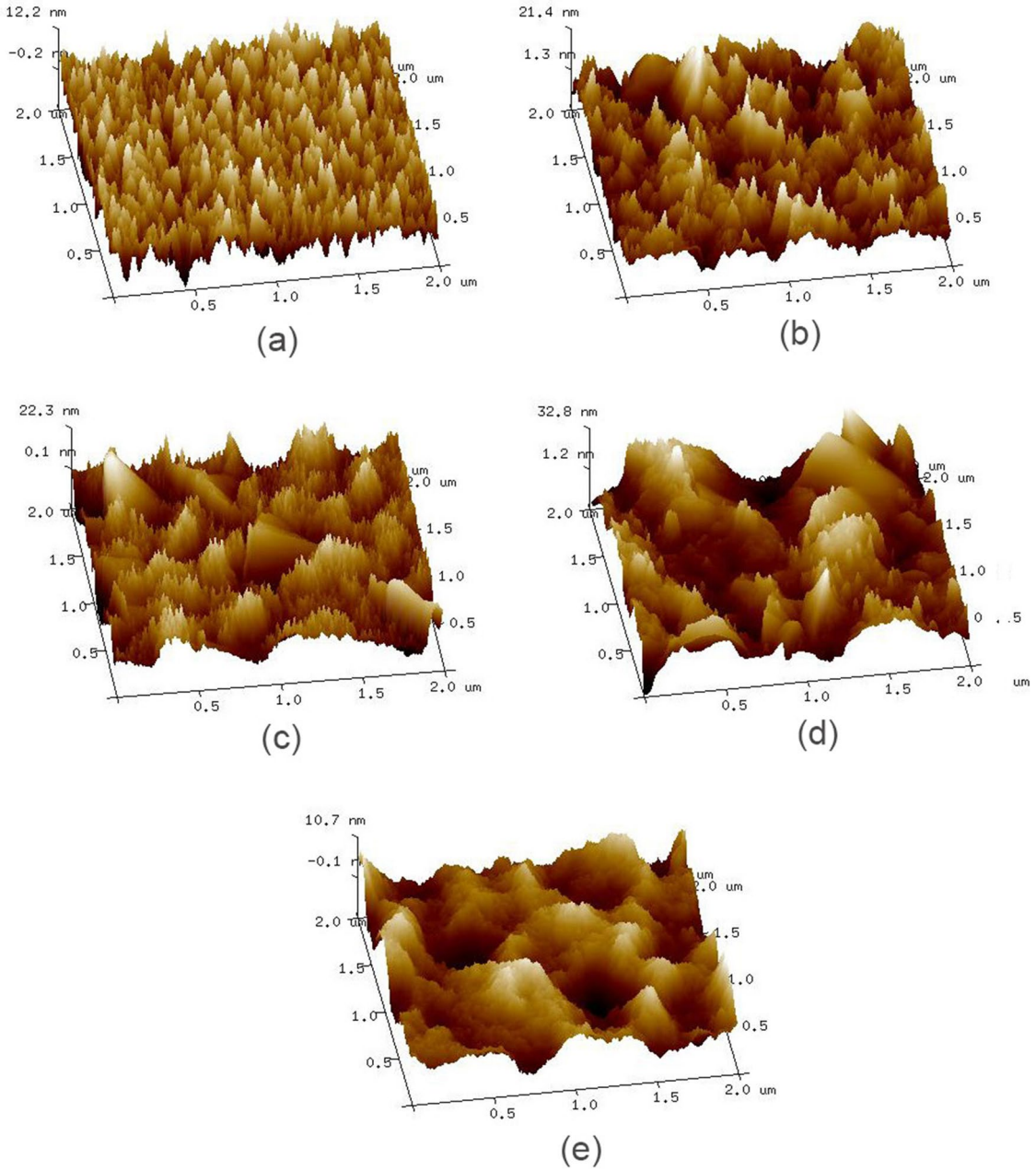

Fig. 1 The AFM images of $Al_{1-x}In_xN$ films with various In contents **a** $x=0.3$, **b** $x=0.55$, **c** $x=0.59$, **d** $x=0.64$, **e** $x=0.7$

The reduction in transmittance intensity is induced by the increase in thickness in $Al_{1-x}In_xN$ films, as has been proved in previous research when increasing the In content [25]. In addition, the interference fringes are observed in the high-transmittance region of each transmission spectrum. This phenomenon is common in the transmission spectrum of semiconductor films prepared by magnetron sputtering due to multiple film-substrate reflections of light [22, 26]. To obtain E_g of the $Al_{1-x}In_xN$ films with different In contents, the Tauc plots from the transmission spectra of $Al_{1-x}In_xN$ films are shown in Fig. 4b. The optical E_g values of $Al_{1-x}In_xN$ films with different In contents are then obtained through the linear extrapolation of the $(\alpha h\nu)^2$ *versus* $h\nu$ curves on the energy axis. This method has been used to measure E_g in semiconductor films [26–28]. The E_g values are estimated to be 2.93, 2.5, 2.25, 2.02, 1.99, and 1.85 eV at In contents of $x=0.3$, 0.41, 0.55, 0.59, 0.64, and 0.7, respectively. The tunable bandgap of as-grown $Al_{1-x}In_xN$ films covers the visible spectrum region (423–670 nm), which indicates its potential for use in visible-light-responsive devices. It should be noted that intrinsic E_g values of In-rich $Al_{1-x}In_xN$ films prepared by RF-MS are not determined accurately. This is because the

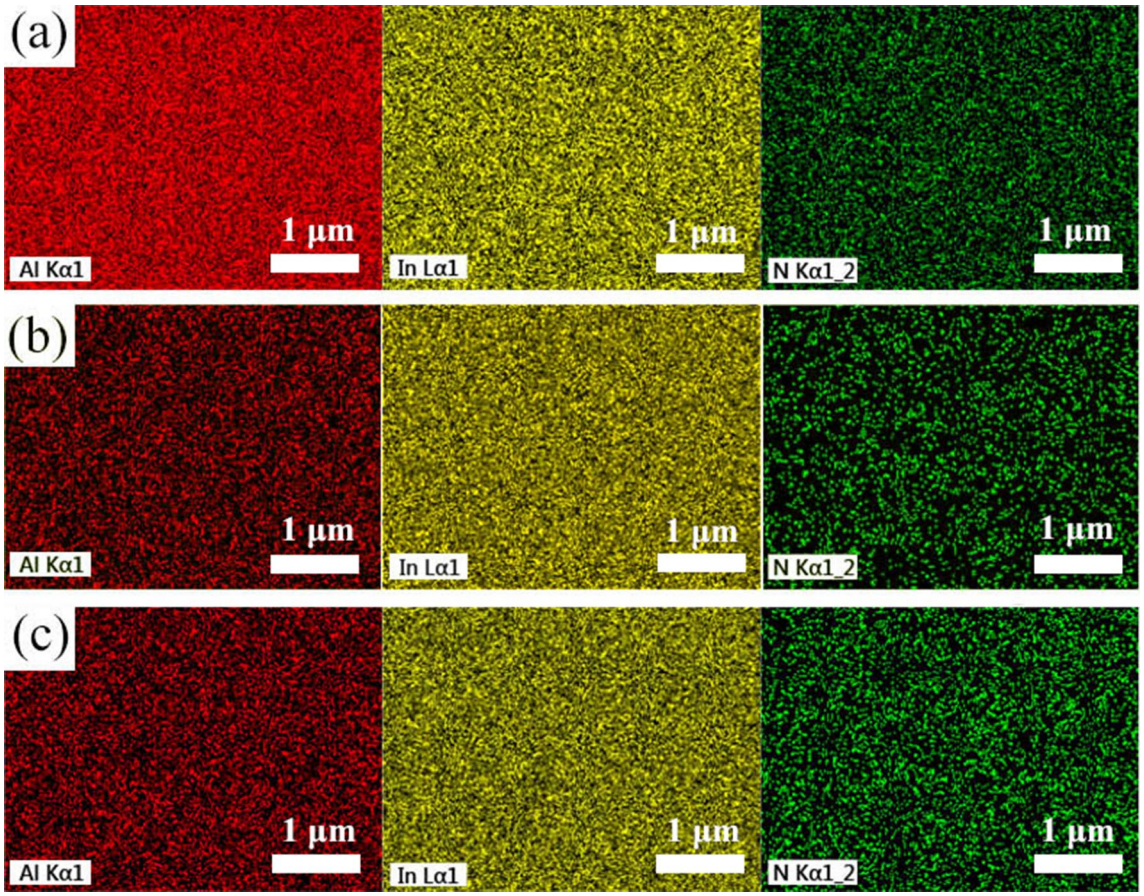

Fig. 2 The Al, In, and N elemental mapping of the surface SEM images for three typical $Al_{1-x}In_xN$ films with In contents: **a** $x=0.3$, **b** $x=0.59$, and **c** $x=0.7$

experimental E_g would be increased with higher carrier concentration (about 10^{20}–10^{21} cm^{-3}) due to the Burstein–Moss effect [22, 24]. This effect arises when the carrier concentration surpasses the conductive band edge density of states and the Fermi level is located within the conductive band. In previous studies, the Burstein–Moss effect inevitably occurred when the electron concentration of InN film exceeded 10^{19} cm^{-3}. However, the electron concentration of as-prepared In-rich $Al_{1-x}In_xN$ films ($x=0.64$ and 0.7) is about 10^{20} cm^{-3} obtained by Hall measurements. Therefore, it is concluded that the obtained E_g of In-rich $Al_{1-x}In_xN$ films (1.99 and 1.85 eV for $x=0.64$ and 0.7, respectively) is higher than intrinsic absorption edge due to Burstein–Moss effect. The speculation is further supported by first-principle calculated value of 1.9 and 1.75 eV for In-rich $Al_{1-x}In_xN$ films ($x=0.64$ and 0.7) [29].

Figure 5 shows the Raman spectra of the as-prepared $Al_{1-x}In_xN$ films with different In contents. In order to follow the evolution of phonon mode, three typical $Al_{1-x}In_xN$ films were measured by Raman scattering. For $Al_{0.36}In_{0.64}$ N film (Blue curve), three main peaks, diversely centring at 521, 618, and 697 cm^{-1}, can be assigned to the E_2(high), InN-like A_1(LO) and AlN-like A_1(LO) phonon modes of wurtzite $Al_{1-x}In_xN$, respectively [30]. With the decrease in In content to 0.55, the peaks shift to high frequency simultaneously. After further reduction in the In content to 0.3, it is noted that the Raman signals of $Al_{0.7}In_{0.3}$ N film are not clear. This phenomenon can be well explained by the resonant excitation effect. The excitation laser energy (2.41 eV) used here is much smaller than the bandgap of $Al_{0.7}In_{0.3}$ N, which leads to the resonant excitation effect reducing and thus results in the weak Raman signals [30].

Figure 6 shows the PL spectra of $Al_{1-x}In_xN$ films with different In contents. They exhibit the broad emission band centred on 2.4, 2.19, 2.06, 1.98, and 1.89 eV at In contents of $x=0.41$, 0.55, 0.59, 0.64, and 0.7, respectively. The emissions show a gradual red shift towards a lower energy with increasing In composition. The evolution of the emission band with the variation of In content is in good agreement with the evidence provided by the transmission spectrum (Fig. 4). The PL emission energy (E_{PL}) is compared with the room-temperature values of E_g, as summarised in Table 1. The values of E_{PL} are close to those of E_g, indicating that the emission band can be attributed to the band edge emission

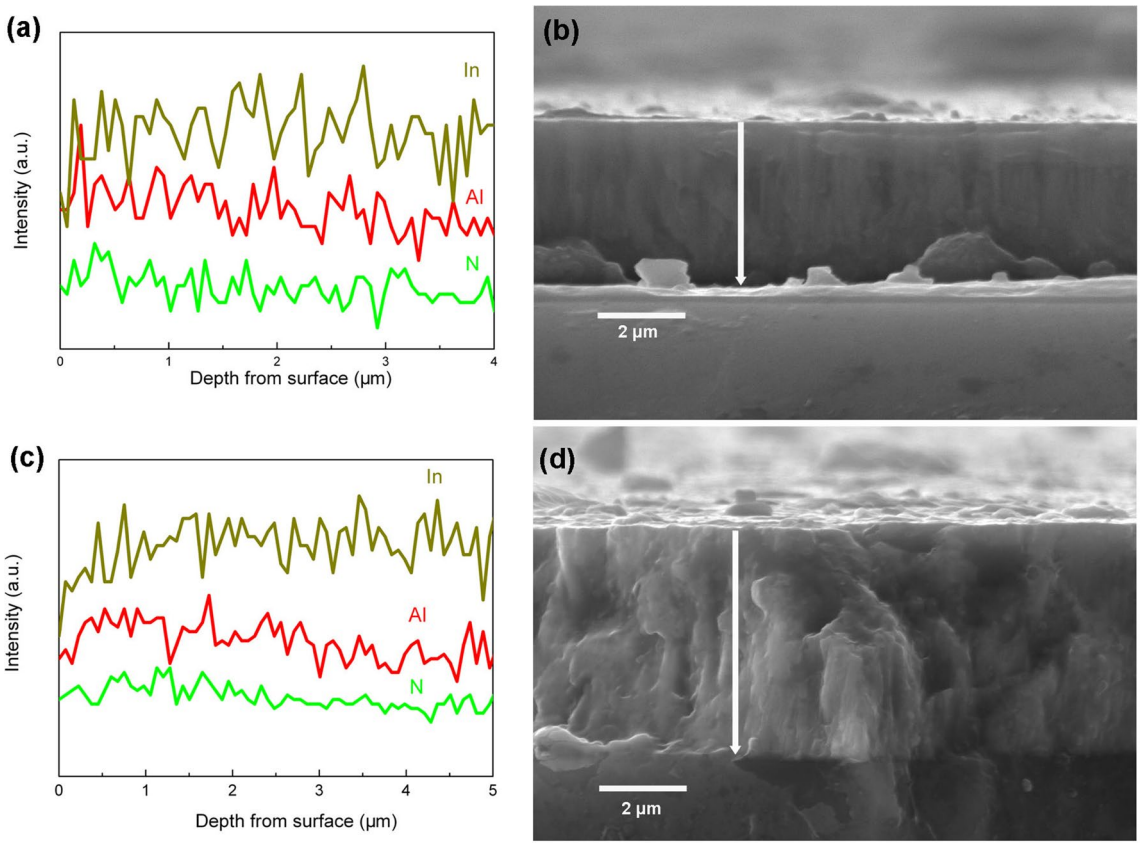

Fig. 3 The line-scan EDS analysis of selected $Al_{1-x}In_xN$ films with different In contents: **a** $x = 0.55$ and **b** corresponding cross-sectional SEM image; **c** $x = 0.59$ and **d** Corresponding cross-sectional SEM image

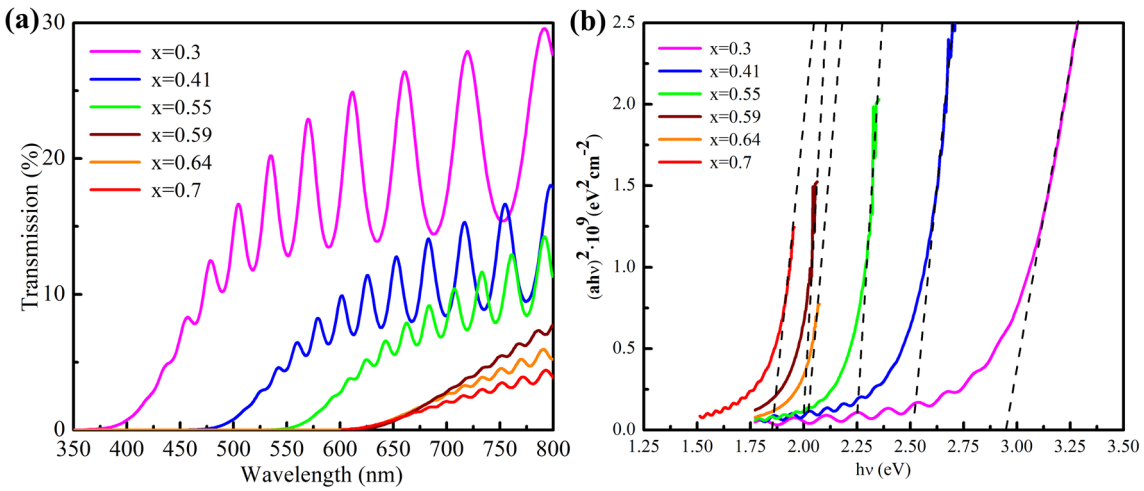

Fig. 4 **a** Optical transmission spectra and **b** plots of $(\alpha h\nu)^2$ *versus* $h\nu$ of $Al_{1-x}In_xN$ films with different In contents

of $Al_{1-x}In_xN$ films. Small deviation (10 ~ 100 meV) between the E_{PL} and E_g can be explained by Stokes shift in $Al_{1-x}In_xN$ film [31]. For the In-rich $Al_{1-x}In_xN$ films, the bandgap energies estimated from Tauc plots are lower than the PL emission energies, which is caused by the weak transmitted light near the bandgap energy for thick samples. The thicknesses of In-rich $Al_{1-x}In_xN$ films can be referred to in our previous study [25].

It is essential to determine E_g of $Al_{1-x}In_xN$ films with different In content for their optoelectronic applications. The

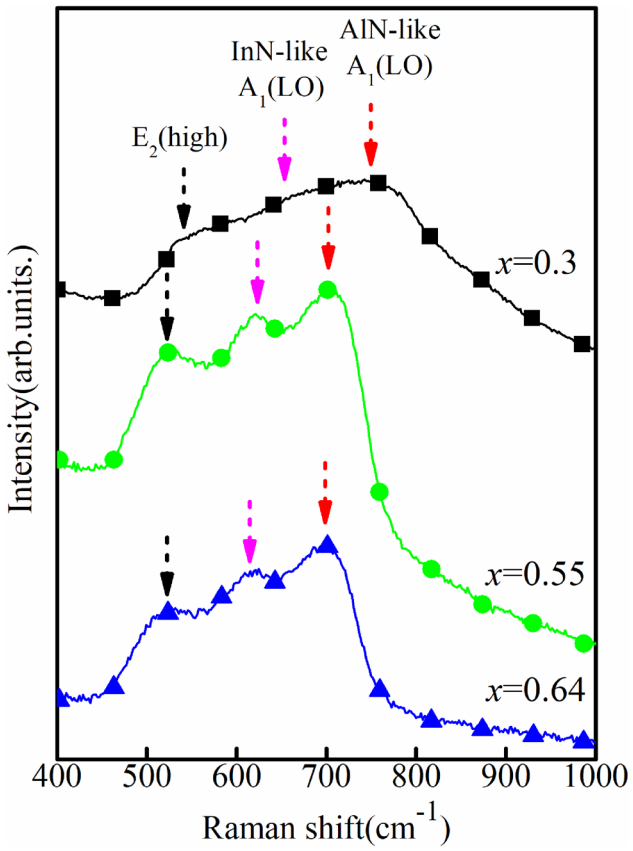

Fig. 5 The Raman spectra of the as-prepared $Al_{1-x}In_xN$ films with different In contents

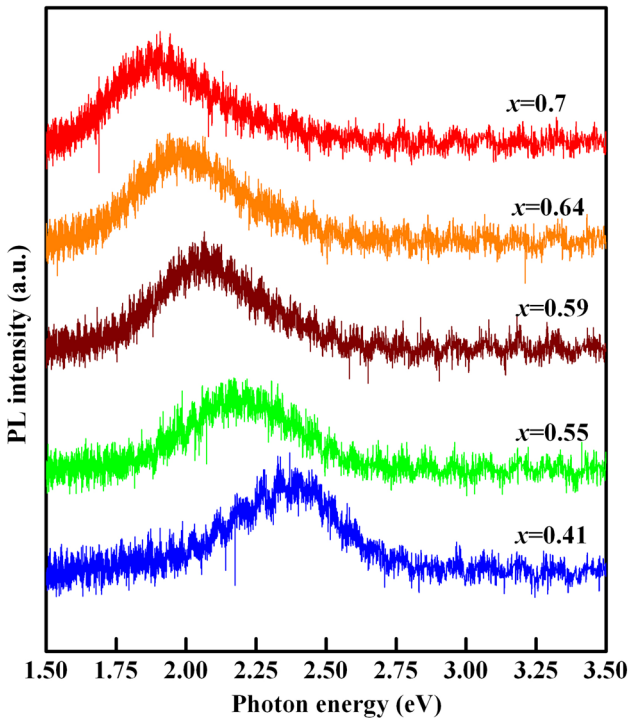

Fig. 6 The PL spectra of $Al_{1-x}In_xN$ films with different In contents

Table 1 Summary of absorption edge (E_g) and PL emission energy (E_{PL}) *versus* In content (x)

x	0.3	0.41	0.55	0.59	0.64	0.7
E_g (eV)	2.93	2.5	2.25	2.02	1.99	1.85
E_{PL}(eV)	~	2.4	2.19	2.06	1.98	1.89

dependence of E_g on In content of the $Al_{1-x}In_xN$ films is shown in Fig. 7. The value of E_g for $Al_{1-x}In_xN$ as a function of the In content is determined by the following bowing equation [29]:

$$E_{AlInN}(x) = xE_{InN} + (1-x)E_{AlN} - bx(1-x) \quad (1)$$

where E_{InN} and E_{AlN} are the bandgap energies of InN and AlN, respectively, and b is the bowing parameter. The bowing parameter of $b = 2.28$ eV is obtained by curve fitting to the experimental data obtained in the present work. The "bowing effect" is attributed to unstable nature of $Al_{1-x}In_xN$ within the miscibility gap, charge exchange between bonds in unordered solid solution and relaxation of bond length [32]. The obtained value of bowing parameter $b = 2.28$ eV is less than the reported values in range of 2.4–5.2 eV in the literature [7, 19, 24, 33]. The large variation of b value is resulted from two reasons [24]. (i) The discrepancy of crystallinity results in local fluctuations of the In content in films due to different deposited techniques. (ii) Different E_g

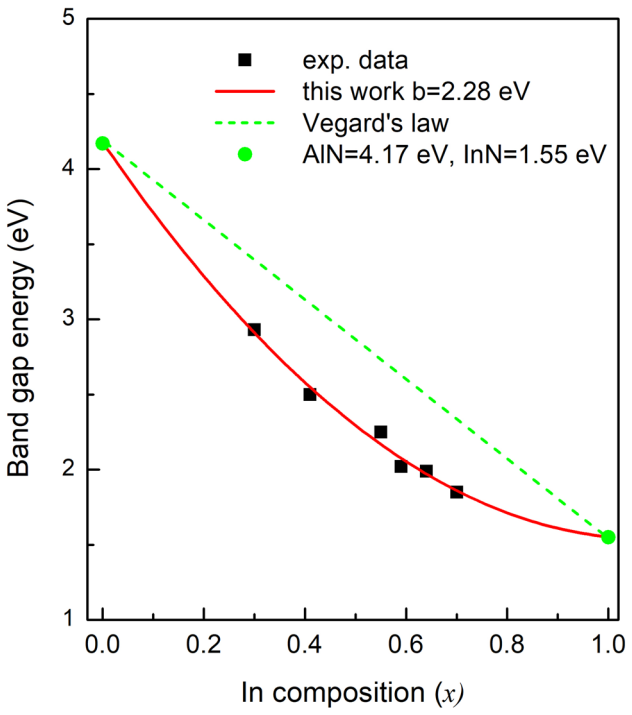

Fig. 7 The dependence of optical bandgap energy on In content of $Al_{1-x}In_xN$ films. We used the values of 0.70 and 6.2 eV for optical bandgaps of InN and AlN, respectively

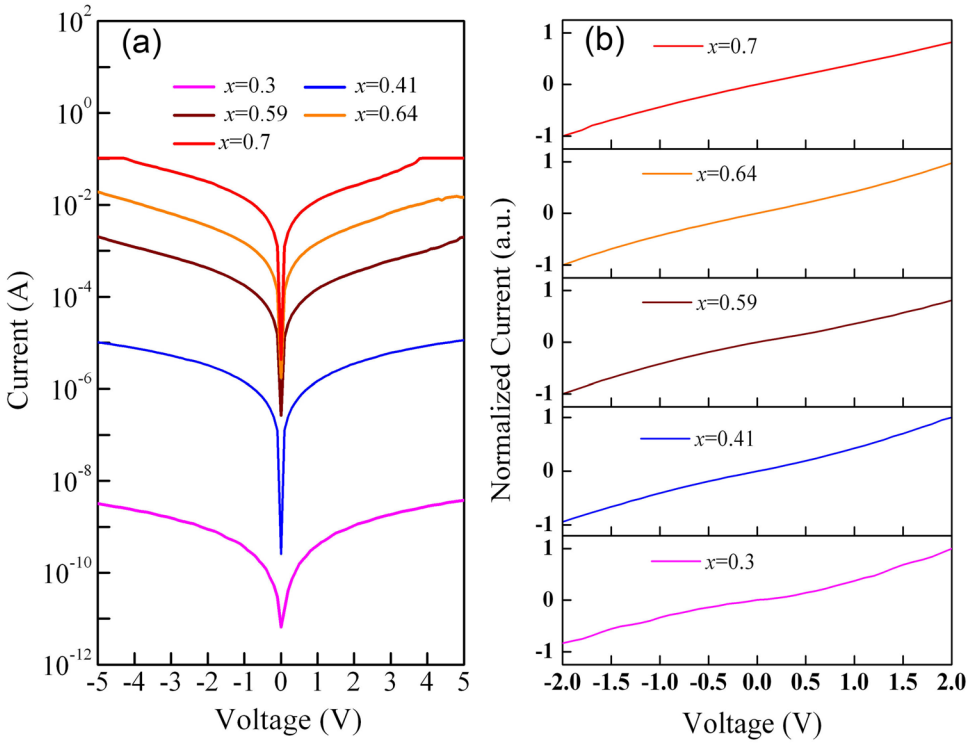

Fig. 8 **a** The semi-log scale I-V curves of the $Al_{1-x}In_xN$ films with different In contents, **b** normalised I-V curves in linear coordinates for $Al_{1-x}In_xN$ films with different In contents with sweep voltage of − 2− + 2 V

values of InN are used for curve fitting. A higher b value is obtained by using small E_g values of InN and vice versa. By extrapolation of fitting curves, the E_g values of InN and AlN are 1.55 eV and 4.17 eV, respectively. The extrapolated E_g of InN (1.55 eV) is in accord with previous reported bandgap of InN films prepared by magnetron sputtering [24]. The extrapolated E_g of AlN (4.17 eV) matches well with the bandgap (4.08 eV) of our sputtered AlN film (Figure S2, Supporting Information). Therefore, for the $Al_{1-x}In_xN$ films prepared by magnetron sputtering, their E_g can be reasonably predicted according to the In content by using our bowing equation ($E_{AlInN}(x) = 2.28x^2\text{-}4.91x + 4.17$).

The I-V curves of the $Al_{1-x}In_xN$ films with different In contents plotted on semi-log axes are shown in Fig. 8a, which shows a very strong composition dependence of the electrical transport properties. With increasing In content, the current increases to a significant extent, which is associated with an increase in carrier concentration. As mentioned above, the Hall measurements confirmed higher electron concentration (about 10^{20} cm^{-3}) in In-rich $Al_{1-x}In_xN$ films ($x = 0.64$ and 0.7). This result agrees with the previous reports, in which a high carrier concentration even over 10^{21} cm^{-3} was obtained in In-rich $Al_{1-x}In_xN$ films [22, 24]. It also supports the conclusion that the carrier concentration increases with the decrease in bandgap in semiconductors. At a bias of + 5 V, the current for In contents $x = 0.3$, 0.41, 0.59, 0.64, and 0.7 is found to be 3.8 nA, 11.37 µA, 2, 14.6, and 105 mA, respectively. From $x = 0.3$ to $x = 0.59$, the increase in current is about 3000 and 175 times for 3.8 nA to 11.37 µA and 11.37 µA to 2 mA, respectively; however, the increases in current from 2 to 14.6 mA and 14.6 to 105 mA were all about 7 times when the content x increases from 0.59 to 0.7. This indicates that the current exhibits a stable, small increase in In-rich $Al_{1-x}In_xN$ films in comparison with those of a low In content. Thanks to the extraordinarily electrical property of $Al_{1-x}In_xN$ film, the $Al_{1-x}In_xN$ films exhibit the potential for the nickel-based electrochemical supercapacitor application [34, 35]. The normalised I-V curves of the $Al_{1-x}In_xN$ films with different In contents are plotted on linear axes in Fig. 8b. All I-V curves show quasi-linear, symmetric features, indicating the formation of quasi-Ohmic contact between metal W electrodes and the $Al_{1-x}In_xN$ films.

4 Conclusion

We investigated the dependence of microstructure, E_g and current–voltage (I-V) characteristics on the In content of $Al_{1-x}In_xN$ films with a wide middle-composition range ($0.3 \le x \le 0.7$). $Al_{1-x}In_xN$ films show the lowest roughness of 2.39 nm at the largest In content of 0.7. A homogeneous compositional distribution is presented in the surface and cross section of $Al_{1-x}In_xN$ films, which confirms no phase separation throughout the composition range. The optical bandgaps of $Al_{1-x}In_xN$ films gradually show a redshift from 2.93 eV ($x = 0.3$) to 1.85 eV ($x = 0.7$) with increasing In content, covering almost the entire visible region. The bowing parameter of 2.28 eV is obtained for as-grown $Al_{1-x}In_xN$

films. The extrapolated values obtained by curve fitting are 4.17 and 1.55 eV for AlN and InN, respectively. The current in these $Al_{1-x}In_xN$ films increases significantly from 3.8 nA to 105 mA with increasing In content. The *I-V* curves show quasi-Ohmic contact behaviour.

Supplementary Information The online version contains supplementary material available at https://doi.org/10.1007/s00339-022-05289-3.

Acknowledgements This work was financially supported by the Natural Science Foundation Guidance Plan Project of Liaoning province (2019-ZD-0254), Opening Foundation of Key Laboratory of Functional Materials Physics and Chemistry of the Ministry of Education (2017004) and Basic Research Program of Educational Commission of Liaoning province (Grant No. LG 201910 and LG 201716). Open Project of State Key Laboratory of Superhard Materials, Jilin University (202004)

Declarations

Conflict of interest The authors declare that they have no conflict of interests or personal relationships that could have appeared to influence the work reported in this paper.

References

1. M.T. Hardy, D.F. Feezell, S.P. DenBaars, S. Nakamura, Mater. Today **14**, 408 (2011)
2. S. Nakamura, Rev. Mod. Phys **87**, 1139 (2015)
3. Y. Kim, M.S. Kim, H.J. Yun, S.Y. Ryu, B.J. Choi, Ceram. Int. **44**, 17447 (2018)
4. M.G. Kibria, H.P.T. Nguyen, K. Cui, S. Zhao, D. Liu, H. Guo, M.L. Trudeau, S. Paradis, A.R. Hakima, Z. Mi, ACS Nano **7**, 7886 (2013)
5. R. Kour, S. Arya, S. Verma, A. Singh, P. Mahajan, A. Khosla, ECS J. Solid State Sci. Technol. **9**, 015011 (2020)
6. S. Khan, S. Arya, P. Lehana, J. Nano- Electron. Phys. **5**, 02010 (2013)
7. C. Besleaga, A.C. Galca, C.F. Miclea, I. Mercioniu, M. Enculescu, G.E. Stan, A.O. Mateescu, V. Dumitru, S. Costea, J. Appl. Phys. **116**, 153509 (2014)
8. S.F. Chichibu, K. Kojima, A. Uedono, Y. Sato, Adv. Mater **29**, 1603644 (2017)
9. M. Alizadeh, G.B. Tong, M.S. Mehmood, K.W. Qader, S.A. Rahman, B. Shokri, Sol. Energy Mater. Sol. Cells **185**, 445 (2018)
10. C. Hums, J. Bläsing, A. Dadgar, A. Diez, T. Hempel, J. Christen, A. Krost, K. Lorenz, E. Alves, Appl. Phys. Lett. **90**, 022105 (2007)
11. H.K. Chauveau, P. Mierry, J.M. Chauveau, J.Y. Duboz, J. Cryst. Growth **316**, 30 (2011)
12. M. Miyoshi, M. Yamanaka, T. Egawa, T. Takeuchi, J. Cryst. Growth **506**, 40 (2019)
13. N. Hatui, M. Frentrup, A.A. Rahman, A. Kadir, S. Subramanian, M. Kneissl, A. Bhattacharya, J. Cryst. Growth **411**, 106 (2015)
14. W.C. Chen, Y.H. Wu, C.Y. Peng, C.N. Hsiao, L. Chang, Nanoscale Res. Lett. **9**, 204 (2014)
15. M. Alizadeh, V. Ganesh, H. Mehdipour, N.F.F. Nazarudin, B.T. Goh, A. Shuhaimi, S.A. Rahman, J. Alloys Compd **632**, 741 (2015)
16. M. Alizadeh, V. Ganesh, A. Pandikumar, B.T. Goh, S. Azianty, N.M. Huang, S.A. Rahman, J. Alloys Compd **670**, 229 (2016)
17. A. Núñez-Cascajero, S. Valdueza-Felip, R. Blasco, M. de la Mata, S.I. Molina, M. González-Herráez, E. Monroy, F.B. Naranjo, J. Alloys Compd **769**, 824 (2018)
18. N. Afzal, M. Devarajan, K. Ibrahim, Mater. Sci. Semicond. Process **51**, 8 (2016)
19. C.J. Dong, M. Xu, Q.Y. Chen, F.S. Liu, H.P. Zhou, Y. Wei, H.X. Ji, J. Alloys Compd **479**, 812 (2009)
20. T.S. Yeh, J.M. Wu, W.H. Lan, Thin Solid Films **517**, 3204 (2009)
21. Q.X. Guo, Y. Okazaki, Y. Kume, T. Tanaka, M. Nishio, H. Ogawa, J. Cryst. Growth **300**, 151 (2007)
22. A. Núñez-Cascajero, S. Valdueza-Felip, L. Monteagudo-Lerma, E. Monroy, E. Taylor-Shaw, R.W. Martin, M. González-Herráez, F.B. Naranjo, J. Phys. D Appl. Phys. **50**, 065101 (2017)
23. A. Núñez-Cascajero, L. Monteagudo-Lerma, S. Valdueza-Felip, C. Navío, E. Monroy, M. González-Herráez, F.B. Naranjo, Jpn. J. Appl. Phys **55**, 05–07 (2016)
24. H. He, Y. Cao, R. Fu, W. Guo, Z. Huang, M. Wang, C. Huang, J. Huang, H. Wang, Appl. Surf. Sci **256**, 1812 (2010)
25. L. Wei, S. Longhai, L. Jun, C. Jianjin, W. Lijun, Q. Dongli, Z. Gang, L. Xuefei, Appl. Surf. Sci **504**, 144335 (2020)
26. F. Wu, X. Tong, Z. Zhao, J. Gao, Y. Zhou, P. Kelly, J. Alloys Compd **695**, 765 (2017)
27. K. Ou, S. Wang, M. Huang, Y. Zhang, Y. Wang, X. Duan, L. Yi, J. Lumin **199**, 34 (2018)
28. A.S. Hassanien, A.A. Akl, Superlatt. Microstruct. **89**, 153 (2016)
29. T. Kawamura, Y. Fujita, Y. Hamaji, T. Akiyama, Y. Kangawa, I. Gorczyca, T. Suski, M. Wierzbowska, S. Krukowski, Phys. Status. Solidi. B **257**, 1900530 (2019)
30. T. Kang, A. Hashimoto, A. Yamamoto, Phys. Rev. B **79**, 033301 (2009)
31. R. Butté, J.F. Carlin, E. Feltin, M. Gonschorek, S. Nicolay, G. Christmann, D. Simeonov, A. Castiglia, J. Dorsaz, H.J. Buehlmann, S. Christopoulos, G. Baldassarri Höger von Högersthal, A.J.D. Grundy, M. Mosca, C. Pinquier, M.A.P.F. Demangeot, J. Frandon, P.G. Lagoudakis, J.J. Baumberg, N. Grandjean, J. Phys. D: Appl. Phys. **40**, 6328 (2007)
32. A.V. Voznyy, V.G. Deibuk, Semiconductors **38**, 304 (2004)
33. T.S. Yeh, J.M. Wu, W.H. Lan, J. Cryst. Growth **310**, 5308 (2008)
34. S. Verma, S. Arya, V. Gupta, A. Khosla, Chem. Eng. J **424**, 130567 (2021)
35. A. Sv, A. Sa, B. Vg, C. Sm, D. Hf, D. Ak, J. Mater. Res .Technol. **11**, 564 (2021)